

Sub- Sm^{-1} electromagnetic induction imaging with an unshielded atomic magnetometer

Cameron Deans,¹ Luca Marmugi,^{1, a)} and Ferruccio Renzoni¹

Department of Physics and Astronomy, University College London, Gower Street, London, WC1E 6BT, UK

(Dated: 4 September 2022)

Progress in electromagnetic induction imaging with atomic magnetometers has brought its domain to the edge of the regime useful for biomedical imaging. However, a demonstration of imaging below the required 1 Sm^{-1} level is still missing. In this Letter, we use an ^{87}Rb radio-frequency atomic magnetometer operating near room temperature in an unshielded environment to image calibrated solutions mimicking the electric conductivity of live tissues. By combining the recently introduced near-resonant imaging technique with a dual radio-frequency coil excitation scheme, we image 5 mL of solutions down to 0.9 Sm^{-1} . We measure a signal-to-noise ratio of 2.7 at 2 MHz for 0.9 Sm^{-1} , increased up to 7.2 with offline averaging. Our work is an improvement of 50 times on previous imaging results, and demonstrates the sensitivity and stability in unshielded environments required for imaging biological tissues, in particular for the human heart.

Recent years have seen a vast increase in the applications of quantum technologies, and in particular atomic magnetometers¹, to the biomedical field. Notable examples include magnetocardiography^{2–5} and magnetoencephalography^{4,6,7}. Applications for monitoring the reactivity of the nervous system have been also reported⁸. In all cases, the superior performance of the atomic magnetometers pushes existing technologies and diagnostic methods towards their fundamental limits.

However, mapping the electric conductivity of biological tissues is still an open issue. Electromagnetic induction imaging – often referred to as magnetic induction tomography⁹ to highlight its tomographic capabilities – has been proposed as a diagnostic tool for various conditions characterized by a variation or an anomaly in electric conduction^{10–13}. With this technique, eddy currents are excited in the specimen under investigation by an AC magnetic field (primary field). The response, containing information about the electric conductivity, electric permittivity, and magnetic permeability of the specimen, is detected via the magnetic field generated by the eddy currents (secondary field). One of the main limitations of this approach is the limited sensitivity of the magnetic field sensors in use. Therefore, until recently, detection and imaging were limited to relatively large samples¹⁴, in most cases well above useful volumes for medical applications. This issue was potentially solved by the demonstration of electromagnetic induction imaging with atomic magnetometers^{15–17}. The higher sensitivity of the core sensor paved the path to applications with small volumes of low-conductivity materials^{18,19}. Nevertheless, a direct demonstration of imaging of sub- Sm^{-1} specimens in unshielded environments, as required for applications in the biomedical field¹⁸, is still lacking.

In this Letter, we demonstrate electromagnetic induction imaging of sub- Sm^{-1} calibrated solutions with an ^{87}Rb radio-frequency (RF) atomic magnetometer operating in an unshielded environment, near room temperature, without

any background subtraction. The performance required for imaging samples mimicking the conductivity of the cardiac tissue^{20,21} ($\sigma_{\text{el}} \sim 0.7 \text{ Sm}^{-1}$ – 0.9 Sm^{-1}) is obtained by combining near-resonant imaging with dual RF coil driving. By using two RF coils in anti-phase, we enhance the sensitivity of the atomic magnetometer to changes in conductivity, without detrimental effects due to RF-induced power broadening. This represents an alternative to increasing the magnetometer's operational frequency. To optimise the imaging performance, we minimized the measured phase noise with a redesigned approach to data collection and programmable near-resonant imaging¹⁸. In this way, we are able to obtain a proof-of-principle demonstration exactly matching the requirements for imaging of cardiac tissue²².

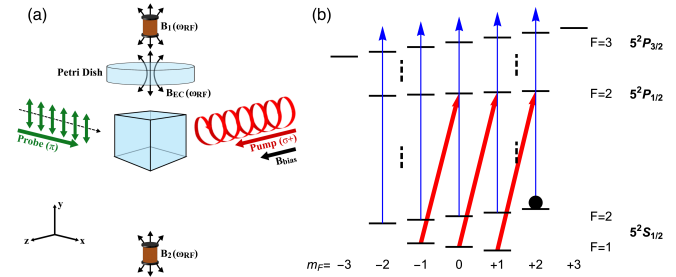


FIG. 1. (a) Schematic of the imaging setup with two RF coils. (b) Energy levels involved in the atomic magnetometer operation.

The experimental setup is a targeted evolution of a previous realization¹⁸. The atomic magnetometer is operated in an unshielded environment, by optically pumping ^{87}Rb atoms in a 25 mm quartz cell (buffer gas: N_2 , 40 Torr) to the $|5^2\text{S}_{1/2}\text{F}=2, m_F=+2\rangle$ state via a σ^+ -polarized laser beam at 795 nm (80 MHz detuning, 330 μW) and a collinear DC bias field. This field (B_{bias} , in Fig. 1(a)) is locked to the desired value, using a three-axis fluxgate (Bartington MAG690), 46 mm away from the center of the vapor cell^{23,24} and a feedback loop. Passive compensation coils nullify DC stray magnetic fields and gradients. The readout of the atomic spin precession is obtained with a π -polarized probe beam, tuned

^{a)}Electronic mail: l.marmugi@ucl.ac.uk

1300 MHz above the $|5^2S_{1/2}F=2\rangle \rightarrow |5^2P_{3/2}F=3\rangle$ transition Fig. 1(b). The probe's polarization plane is continuously monitored by a polarimeter, whose output is analyzed by a lock-in amplifier (Zurich Instruments HF2LI). Larmor precession of atomic spins is driven by an RF magnetic field ($\mathbf{B}_1(\omega_{RF}) + \mathbf{B}_2(\omega_{RF})$) in Fig. 1(a)). The RF field is provided by a pair of 100 μ H coils, of diameter 7.8 mm. They are placed at ± 47 mm with respect to the center of the vapor cell, in an arrangement similar to those recently used in other atomic magnetometer setups^{19,25}, implementing the idea of Watson *et al.*²⁶. The coils are antiparallel along the same axis. This creates two AC fields oscillating at the same frequency and with stable π phase difference (anti-phase). The object to be imaged is placed between the top coil and the sensor, 40 mm above its center (Fig. 1(a)).

The RF magnetic field – $\mathbf{B}_1(\omega_{RF}) + \mathbf{B}_2(\omega_{RF})$, the primary field – induces eddy currents in the object. These produce a secondary magnetic field ($\mathbf{B}_{EC}(\omega_{RF})$ in Fig. 1(a)), oscillating at the same frequency, and containing information about the properties of the object⁹. By moving the specimen, held in position by a motorized PLA and Nylon support, with respect to the sensor and measuring its response at desired position, 2D images are obtained.

One issue with electromagnetic induction imaging and atomic magnetometers are the contrasting requirements for the amplitude of the RF field. Increasing the amplitude of the primary field at the object's position proportionally increases the secondary field to be detected¹⁰. In contrast, increasing the amplitude of the driving field causes RF-induced power broadening, and a consequent reduction of the magnetometer's sensitivity²³. The dual RF coil, driven in parallel by the local oscillator of the lock-in amplifier, allows us to increase the amplitude of the RF field by more than 15 times at the object's level (the driving voltage for the RF coils is increased from $V_{RF}=0.6$ V to $V_{RF}=10$ V), without broadening the atomic resonances (Fig. 2). In this way, extremely low conductivity specimens can be imaged in unshielded environments, without the need to increase the frequency¹⁸. We did not completely cancel the response of the magnetometer (Fig. 2), instead creating a small imbalance in the currents flowing the two branches of the circuit (split ratio $\sim 51\%:49\%$). This allows near-resonant imaging to be used. A different approach to long-term stability for electromagnetic induction imaging was recently demonstrated with a self-oscillating spin maser²⁷.

Calibrated conductivity solutions, contained in Petri dishes (Star Lab CytOne Dish, diameter 35 mm, height 10 mm), are used. The range of conductivities was chosen to mimic live biological tissues. The specimens were independently assessed with a Jenway 4510 conductivity meter and a Jenway 027 213 Epoxy Bodied probe, at the temperature and time of imaging. We present results using three levels of conductivity: 1) $(9.1 \pm 0.1) \text{ S m}^{-1}$ at $(20.1 \pm 0.1)^\circ\text{C}$, Reagecon CSKC100M (batch CS100M19H1); 2) $(4.5 \pm 0.1) \text{ S m}^{-1}$ at $(20.0 \pm 0.1)^\circ\text{C}$, obtained with an NaCl (Sigma-Aldrich Redi-Dri reagent, $\geq 99\%$ purity, 746398-500G) and de-ionized water (RS PRO De-ionized water, 251-3687) solution; 3) $(0.91 \pm 0.01) \text{ S m}^{-1}$ at $(20.2 \pm 0.1)^\circ\text{C}$, Reagecon CSKC10M

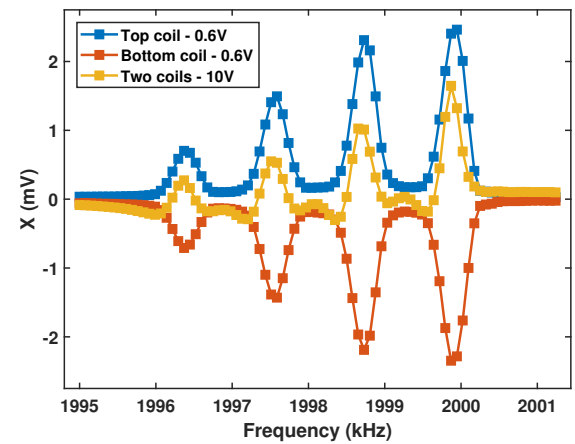


FIG. 2. Comparison of the in-phase (X) response with the top, bottom, and dual coils driving the AM for $V_{RF}=0.6$ V, 0.6 V, and 10 V, respectively.

(batch CS10M19B2). Other tests were conducted with NaCl solutions at different concentrations. No noticeable difference in the response of different solutions with the same conductivity is detected. This suggests that the imaging process is independent of the chemical details of the solution and of the ionic carrier. The Petri dishes are filled with (5.0 ± 0.2) mL of solution, and then sealed to prevent evaporation. For imaging, we

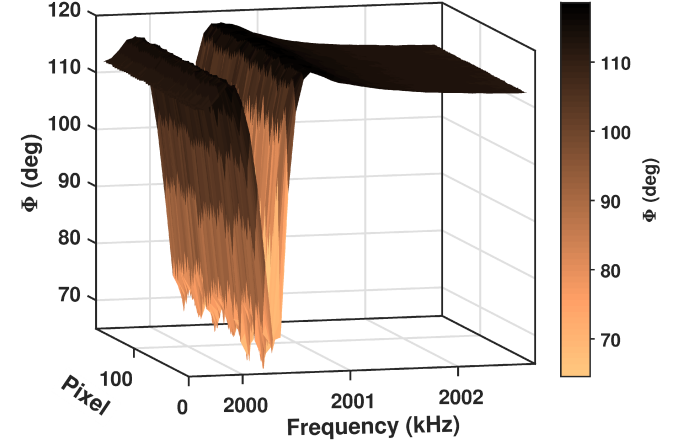


FIG. 3. Phase (Φ) spectra as a function of the RF frequency collected for a typical image. A complete image acquisition is constituted by X, Y, R, and Φ spectra per each pixel of the 2D imaging area.

operate the magnetometer at a fixed frequency of 2 MHz. To maximize the amount of the retained information, the system automatically acquires a full RF spectrum at each position of the image (i.e. for each pixel), by sweeping the RF field frequency across the atomic resonance. Five arrays, containing the swept frequency, the in-phase response (X), the quadrature response (Y), the amplitude of the response (R), and its phase lag (Φ) are collected during the scan. For an $n \times m$ pixels scan and a k -points long frequency scan, five matrices are

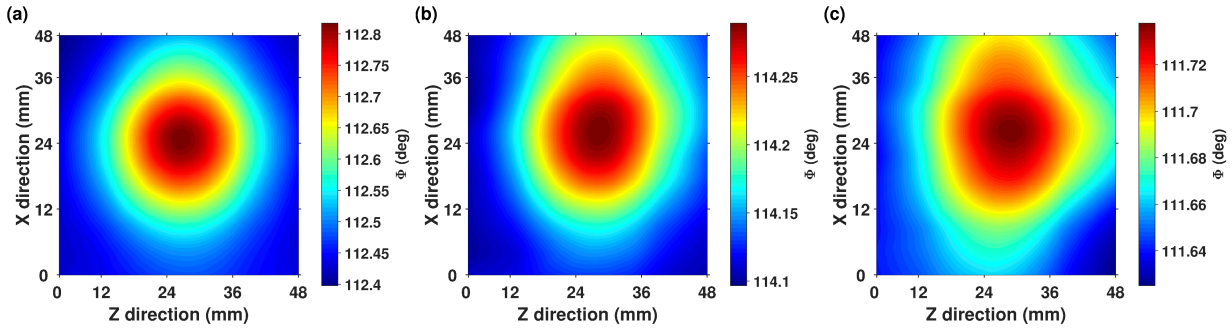


FIG. 4. Imaging of low-conductivity 5 ml calibrated solutions. (a) Phase image of the $(9.1 \pm 0.1) \text{ S m}^{-1}$ sample. (b) Phase image of the $(4.5 \pm 0.1) \text{ S m}^{-1}$ sample. (c) Phase image of the $(0.91 \pm 0.01) \text{ S m}^{-1}$ sample.

thus stored, each formed by k columns and $(n \cdot m)$ rows. As an example, Fig. 3 illustrates the typical raw Φ data obtained by the system. In this case, each pixel is represented by a Φ spectrum of the atomic resonance recorded at that position. In this way, images are obtained for all parameters. This approach allows the automatic implementation of near-resonant imaging¹⁸ at a programmable detuning that minimizes the impact of magnetic noise in the parameter of interest. In the case of the Φ maps presented here, images can be obtained at the near-resonant frequency exhibiting the minimum slope of the phase response. We found the optimum performance at 2 MHz was $+0.7 \text{ kHz}$ from the nominal resonance of the system. Multi-frequency imaging is also automatically attainable. Contrary to our previous demonstration¹⁸, here the optimization can be performed exclusively based on image quality without any intervention on the hardware. In addition, the complete set of raw data is fully retained for further analysis or performance enhancement.

In Fig. 4, we show the Φ maps of three Petri dishes containing 5 ml of calibrated solutions, at 9.1 S m^{-1} (a), 4.5 S m^{-1} (b), and 0.91 S m^{-1} (c). The specimens under investigation are correctly detected, imaged, and located in the scene, within the 4 mm step-size of the translational stage in use. Minor distortions appear in the 0.91 S m^{-1} sample (Fig. 4(c)).

This result is the first example of electromagnetic induction imaging with an atomic magnetometer of small volumes of sub- S m^{-1} specimens. The solutions mimic the ionic conductivity typical of live tissues, where electrolytes move in the intra- and intercellular spaces²⁰. Figure 4(c) demonstrates the feasibility of imaging of the heart with non-invasive electromagnetic induction imaging with atomic magnetometers: the electric conductivity of the healthy cardiac tissue in the MHz range varies^{20,21} between 0.7 S m^{-1} and 0.9 S m^{-1} . This represents the background conductivity on which anomalous structures supporting atrial fibrillation, and speculated to be characterized by an increase in conductivity^{22,28}, emerge. The demonstrated performance of our instrument is thus sufficient for their detection. This, together with the unshielded and automated operation, allows one to conclude that the feasibility of electromagnetic induction imaging of biological tissues is now fully demonstrated.

The minimum imaged conductivity is improved by more than 50 times with respect to previous results¹⁸, and by a fac-

tor 4 with respect to the recently reported detection of low-conductivity solutions in a shielded environment¹⁹. However, when considering the sensitivity of electromagnetic induction imaging instrumentation, the effective volume supporting eddy currents and thus contributing to the generation of the secondary field is also relevant. The larger the volume exhibiting a given conductivity, the bigger is the signal produced. By assuming the most favourable conditions – namely when the skin depth is larger than the thickness of the object and the transverse size of the primary field at the specimen's surface is of the same order of the object's size – one can simply take into consideration its physical volume (V). Following this reasoning, we introduce a figure-of-merit to characterize the absolute conductivity sensitivity of systems performing electromagnetic induction imaging:

$$\mathcal{S} \equiv \sigma_{\text{el}} \cdot V \quad [\text{S m}^2], \quad (1)$$

where σ_{el} is the electric conductivity of the object of interest. Based on Eq. 1, our record performance with the $\sigma_{\text{el}}=0.91 \text{ S m}^{-1}$ sample of $V = 5.0 \text{ mL}$ yields $\mathcal{S} = 4.55 \times 10^{-6} \text{ S m}^2$, an improvement of more than two orders of magnitude over our previous work¹⁸ ($\mathcal{S} = 3.13 \times 10^{-4} \text{ S m}^2$), and of an order of magnitude with respect to recent detection reports¹⁹ ($\mathcal{S} \approx 3.0 \times 10^{-5} \text{ S m}^2$). The $\sigma_{\text{el}}=4.5 \text{ S m}^{-1}$ sample corresponds to $\mathcal{S} = 2.25 \times 10^{-5} \text{ S m}^2$, $\sim 26\%$ better than previous works.

\mathcal{S} also highlights the potential of the unshielded electromagnetic induction imaging with an RF atomic magnetometer with respect to other approaches. Detection of conductivities as low as 0.5 S m^{-1} has been reported with standard coils¹⁴. However, the comparatively large volumes ($2.3 \times 10^3 \text{ mL}$) of the samples gives $\mathcal{S} = 1.13 \times 10^{-3} \text{ S m}^2$, three orders of magnitude worse than the level demonstrated here. Furthermore, nitrogen-vacancy (NV) center magnetometers performing electromagnetic induction imaging²⁹ only conveys $\mathcal{S} \approx 1.8 \times 10^{-1} \text{ S m}^2$, to date.

We have also investigated the performance with various images of identical samples acquired across several hours. The single-image signal-to-noise ratio (SNR) is well above unity in all cases. For the 9.1 S m^{-1} sample, we measured a SNR=13.4. For the 4.5 S m^{-1} sample, SNR=8.0. Fi-

nally, the 0.91 S m^{-1} sample's images exhibit a single-image SNR=2.74.

We have also explored the direct averaging of the images, to improve the signal-to-noise ratio and readability. This would not be necessary when computer algorithms or machine learning are used³⁰. Images in Fig. 4 are obtained by weighted average of several images captured in the same conditions. The weights are given by a normal distribution fit to the set of images. Long-term performance as well as stability and repeatability of imaging – all critical features for imaging relying on unshielded atomic magnetometers – can be tested and quantified. Averaging several images improves such numbers, as expected: the averaged signal-to-noise ratio, $\langle \text{SNR} \rangle$, is 35.5, 16.2, and 7.23 from the three conductivities used, with an improvement of around 2.6 times.

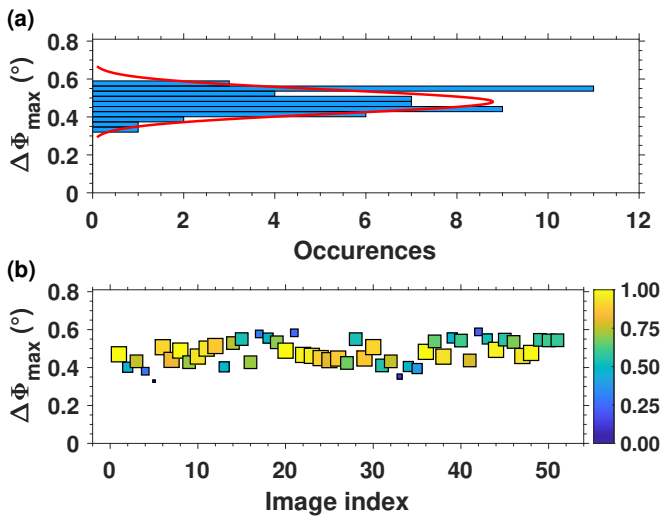


FIG. 5. Stability of sub- S m^{-1} imaging. (a) Distribution of the maximum recorded phase change ($\Delta\Phi_{\text{max}}$) across 51 images images of the 0.91 S m^{-1} sample. The red line is the fitting normal distribution. (b) Corresponding scatter plot. Size and color are proportional to the weight used for averaging. The colorbar indicates the weights [0, 1] attributed to the images.

As an illustration of the stability of the imaging for the 0.91 S m^{-1} sample, we show the distribution of the maximum phase difference measured across an image $\Delta\Phi_{\text{max}}$ for 51 repetitions (Fig. 5(a)):

$$\Delta\Phi_{\text{max}} = (\Phi_{\text{max}} - \Phi_{\text{min}})_{\text{image}}. \quad (2)$$

This allows one to immediately identify issues with the instrument or of the imaging process. The dataset is well-fitted by a normal distribution, with mean value $\langle \Delta\Phi_{\text{max}} \rangle = 0.48^\circ$ with 95 % confidence interval $[0.46^\circ, 0.50^\circ]_{0.95}$ and standard deviation $\sigma = 0.06^\circ$ ($[0.05^\circ, 0.08^\circ]_{0.95}$). In Fig. 5(b) the effect of the weighted average for Fig. 4(c) is illustrated. Once the distribution of the images dataset is identified, it is used for weighting the contribution of the single images to the average.

In conclusion, we have presented electromagnetic induction images of calibrated solutions of conductivities down to the sub- S m^{-1} with an unshielded RF atomic magnetometer. The simultaneous use of near-resonance imaging and of

a dual RF coil excitation provided the necessary sensitivity and stability to allow us to image 5 mL of 0.91 S m^{-1} solution, in magnetically unshielded environments. Our atomic magnetometer-based imaging system operates with sufficient stability to guarantee consistent imaging performance across several days. Based on our results, the feasibility of practical use of electromagnetic induction imaging with atomic magnetometers in the biomedical field is finally fully demonstrated. In particular, direct, non-invasive imaging of the cardiac tissue – for example for the diagnosis of atrial fibrillation²² – has been proven technically feasible.

ACKNOWLEDGMENTS

This work was supported by the UK Quantum Technology Hub in Sensing and Metrology, Engineering and Physical Sciences Research Council (EPSRC) (EP/M013294/1). We thank Dr Helena Wong and Prof Andrea Sella (UCL Department of Chemistry) for the loan of the conductivity meter and guidance on its operation.

- ¹D. Budker and M. Romalis, "Optical magnetometry," *Nature Physics* **3**, 227 EP – (2007).
- ²J. Belfi, G. Bevilacqua, V. Biancalana, S. Cartaleva, Y. Dancheva, and L. Moi, "Cesium coherent population trapping magnetometer for cardiosignal detection in an unshielded environment," *J. Opt. Soc. Am. B* **24**, 2357–2362 (2007).
- ³G. Bison, N. Castagna, A. Hofer, P. Knowles, J.-L. Schenker, M. Kasprzak, H. Saudan, and A. Weis, "A room temperature 19-channel magnetic field mapping device for cardiac signals," *Applied Physics Letters* **95**, 173701 (2009), <https://doi.org/10.1063/1.3255041>.
- ⁴V. K. Shah and R. T. Wakai, "A compact, high performance atomic magnetometer for biomedical applications," *Physics in Medicine and Biology* **58**, 8153–8161 (2013).
- ⁵K. Jensen, M. A. Skarsfeldt, H. Stærkind, J. Arnbak, M. V. Balabas, S.-P. Olesen, B. H. Bentzen, and E. S. Polzik, "Magnetocardiography on an isolated animal heart with a room-temperature optically pumped magnetometer," *Scientific Reports* **8**, 16218 (2018).
- ⁶H. Xia, A. Ben-Amar Baranga, D. Hoffman, and M. V. Romalis, "Magnetoencephalography with an atomic magnetometer," *Applied Physics Letters* **89**, 211104 (2006), <https://doi.org/10.1063/1.2392722>.
- ⁷E. Boto, N. Holmes, J. Leggett, G. Roberts, V. Shah, S. S. Meyer, L. D. Muñoz, K. J. Mullinger, T. M. Tierney, S. Bestmann, G. R. Barnes, R. Bowtell, and M. J. Brookes, "Moving magnetoencephalography towards real-world applications with a wearable system," *Nature* **555**, 657–661 (2018).
- ⁸G. Z. Iwata, Y. Hu, T. Sander, M. Muthuraman, V. C. Chirumamilla, S. Groppa, D. Budker, and A. Wickenbrock, "Biomagnetic signals recorded during transcranial magnetic stimulation (tms)-evoked peripheral muscular activity," *arXiv preprint arXiv:1909.11451* (2019).
- ⁹H. Griffiths, "Magnetic induction tomography," *Measurement Science and Technology* **12**, 1126 (2001).
- ¹⁰H. Griffiths, W. R. Stewart, and W. Gough, "Magnetic induction tomography: A measuring system for biological tissues," *Annals of the New York Academy of Sciences* **873**, 335–345 (1999).
- ¹¹R. Merwa, K. Hollaus, O. Biró, and H. Scharfetter, "Detection of brain oedema using magnetic induction tomography: a feasibility study of the likely sensitivity and detectability," *Physiological Measurement* **25**, 347–354 (2004).
- ¹²M. Zolgharni, H. Griffiths, and P. D. Ledger, "Frequency-difference MIT imaging of cerebral haemorrhage with a hemispherical coil array: numerical modelling," *Physiological Measurement* **31**, S111–S125 (2010).
- ¹³W. Pan, Q. Yan, M. Qin, G. Jin, J. Sun, X. Ning, W. Zhuang, B. Peng, and G. Li, "Detection of cerebral hemorrhage in rabbits by time-difference magnetic inductive phase shift spectroscopy," *PLOS ONE* **10**, 1–14 (2015).

¹⁴H. Griffiths, W. Gough, S. Watson, and R. J. Williams, "Residual capacitive coupling and the measurement of permittivity in magnetic induction tomography," *Physiological Measurement* **28**, S301 (2007).

¹⁵A. Wickenbrock, S. Jurgilas, A. Dow, L. Marmugi, and F. Renzoni, "Magnetic induction tomography using an all-optical 87rb atomic magnetometer," *Opt. Lett.* **39**, 6367–6370 (2014).

¹⁶C. Deans, L. Marmugi, S. Hussain, and F. Renzoni, "Electromagnetic induction imaging with a radio-frequency atomic magnetometer," *Applied Physics Letters* **108**, 103503 (2016).

¹⁷A. Wickenbrock, N. Leefer, J. W. Blanchard, and D. Budker, "Eddy current imaging with an atomic radio-frequency magnetometer," *Applied Physics Letters* **108**, 183507 (2016), <https://doi.org/10.1063/1.4948534>.

¹⁸L. Marmugi, C. Deans, and F. Renzoni, "Electromagnetic induction imaging with atomic magnetometers: Unlocking the low-conductivity regime," *Applied Physics Letters* **115**, 083503 (2019), <https://doi.org/10.1063/1.5116811>.

¹⁹K. Jensen, M. Zugenmaier, J. Arnbak, H. Starkind, M. V. Balabas, and E. S. Polzik, "Detection of low-conductivity objects using eddy current measurements with an optical magnetometer," *Phys. Rev. Research* **1**, 033087 (2019).

²⁰S. Gabriel, R. W. Lau, and C. Gabriel, "The dielectric properties of biological tissues: III. Parametric models for the dielectric spectrum of tissues," *Physics in Medicine and Biology* **41**, 2271–2293 (1996).

²¹T. J. C. Faes, H. A. van der Meij, J. C. de Munck, and R. M. Heethaar, "The electric resistivity of human tissues (100 Hz-10 MHz): a meta-analysis of review studies," *Physiological Measurement* **20**, R1–R10 (1999).

²²L. Marmugi and F. Renzoni, "Optical magnetic induction tomography of the heart," *Scientific Reports* **6**, 23962 EP – (2016).

²³C. Deans, L. Marmugi, and F. Renzoni, "Sub-picotesla widely tunable atomic magnetometer operating at room-temperature in unshielded environments," *Review of Scientific Instruments* **89**, 083111 (2018), <https://doi.org/10.1063/1.5026769>.

²⁴P. Bevington, R. Gartman, and W. Chalupczak, "Imaging of material defects with a radio-frequency atomic magnetometer," *Review of Scientific Instruments* **90**, 013103 (2019), <https://doi.org/10.1063/1.5053959>.

²⁵P. Bevington, R. Gartman, and W. Chalupczak, "Enhanced material defect imaging with a radio-frequency atomic magnetometer," *Journal of Applied Physics* **125**, 094503 (2019), <https://doi.org/10.1063/1.5083039>.

²⁶S. Watson, A. Morris, R. J. Williams, H. Griffiths, and W. Gough, "A primary field compensation scheme for planar array magnetic induction tomography," *Physiological Measurement* **25**, 271–279 (2004).

²⁷P. Bevington, R. Gartman, and W. Chalupczak, "Alkali-metal spin maser for non-destructive tests," *Applied Physics Letters* **115**, 173502 (2019), <https://doi.org/10.1063/1.5121606>.

²⁸C. Deans, L. Marmugi, S. Hussain, and F. Renzoni, "Optical atomic magnetometry for magnetic induction tomography of the heart," *Proc.SPIE* **9900**, 9900 – 9900 – 10 (2016).

²⁹G. Chatzidrosos, A. Wickenbrock, L. Bougas, H. Zheng, O. Tretiak, Y. Yang, and D. Budker, "Eddy-current imaging with nitrogen-vacancy centers in diamond," *Phys. Rev. Applied* **11**, 014060 (2019).

³⁰C. Deans, L. D. Griffin, L. Marmugi, and F. Renzoni, "Machine learning based localization and classification with atomic magnetometers," *Phys. Rev. Lett.* **120**, 033204 (2018).